Iodide-Induced Differential Control of Metal Ion Reduction Rates: Synthesis of Terraced Palladium-Copper Nanoparticles with Dilute Bimetallic Surfaces

*Melissa E. King and Michelle L. Personick**

Department of Chemistry, Wesleyan University, Middletown, Connecticut 06459, United States

Email: mpersonick@wesleyan.edu

Abstract

Metal nanoparticles possessing a high density of atomic steps and edge sites provide an increased population of undercoordinated surface atoms, which can enhance the catalytic activity of these materials compared to low-index faceted or bulk materials. Simply increasing reactivity, however, can lead to a concurrent increase in undesirable, non-selective side products. The incorporation of a second metal at these reactive stepped features provides an ideal avenue for finely attenuating reactivity to increase selectivity. A major challenge in synthesizing the bimetallic nanomaterials with tunable surface features that are desirable for fundamental catalytic studies is a need to bridge differences in precursor reduction potentials and metal lattice parameters in structures containing both a noble metal and a non-noble metal. We report the use of low micromolar concentrations of iodide ions as a means of differentially controlling the relative reduction rates of a noble metal (palladium) and a non-noble metal (copper). The iodide in this system increases the rate of reduction of palladium ions while concurrently slowing the rate of copper ion reduction, thus providing a degree of control that is not achievable using most other reported means of tuning metal ion reduction rate. This differential control of metal ion reduction afforded by iodide ions enables access to nanoparticle growth conditions in which control of palladium nanoparticle growth by copper underpotential deposition becomes possible, leading to the generation of unique terraced bimetallic particles. Because of their bimetallic surface composition, these terraced nanoparticles exhibit increased selectivity to acetaldehyde in gas phase ethanol oxidation.

Introduction

The synthesis of well-defined metal nanoparticles with complex shapes that range beyond Platonic solids has been the focus of ongoing research in nanoparticle synthesis due to the potential applications of these exotic structures in plasmonics[1-6] and catalysis.[7-12] For catalytic applications, bimetallic particles are especially favorable because they offer additional tunability of surface composition, which can lead to greater activity and selectivity. The increased functional flexibility of bimetallic particles relative to their monometallic counterparts may be attributed to the synergistic effects that result from coupling the individual properties of each metal.[13-21] For example, platinum is an effective and active catalyst for the electrocatalytic oxidation of small organic molecules, however, it has been shown that bimetallic structures show greater sustained catalytic activity due to decreased surface poisoning in the presence of a secondary metal such as lead or bismuth.[22] Moreover, the deposition of a dilute surface coverage of a secondary metal is advantageous for strategically enhancing or attenuating the activity of the underlying metal in order to promote higher catalytic selectivity.[17, 23] The prospect of enhanced catalyst performance due to cooperative interactions at bimetallic surfaces has motivated the synthesis of a number of bimetallic noble metal nanoparticle structures—including concave cubes, stellated octahedra, concave hexoctahedra, and trisoctahedra—that are comprised of various binary combinations of the metals gold, palladium, platinum, and silver.[14, 24-27] Such particles may have alloyed or core-shell structures. Shaped nanoparticles with certain bimetallic compositions, such as silver-gold and palladium-platinum, can be more readily synthesized due to the small lattice mismatch between these pairs of noble metals.

The realization of polyhedral bimetallic nanostructures that incorporate less noble metals, however, has been an ongoing challenge because these catalytically relevant metals generally have

a substantial lattice mismatch with noble metals, which leads to ill-defined particles with dendrite or island formation.[28, 29] The incorporation of a second, less noble, metal during nanoparticle synthesis also has a distinct possibility of causing undesired galvanic exchange in which the noble metal completely displaces the secondary metal of interest in the final particle morphology. This galvanic exchange process is sometimes used in an intentional, controlled manner to circumvent issues that arise from the lattice mismatch between two noble metals.[30-33] Copper or lead, for example, can be deposited electrochemically via underpotential deposition onto pre-synthesized metal nanoparticles to serve as a sacrificial metal that will undergo galvanic exchange with a more noble metal to produce core-shell structures with controllable shell thicknesses.[26] Importantly, underpotential deposition may also be employed directly during non-electrochemical colloidal synthesis to control particle morphology and generate bimetallic surface compositions. Underpotential deposition, in which metal ions are reduced onto the surface of a host metal at a potential more positive than their Nernst potential, yields a sub-monolayer to monolayer coverage of a secondary metal at the particles' surface.[34] These underpotentially deposited atoms have been shown to stabilize high-energy surface features such as step edges. As a result, underpotential deposition of silver or copper has proven to be a powerful tool in the solution-phase colloidal synthesis of high-index faceted bimetallic gold nanostructures, such as concave cubes, ditetragonal prisms, and tetrahexahedra.[35-39] Conversely, the underpotential deposition of copper onto the surface of palladium nanoparticles without employing electrochemical methods has been challenging due to the low reduction potential of copper.

Herein, we report a solution-phase colloidal method for the synthesis of terraced palladium particles possessing stepped surface features that are stabilized by underpotentially deposited copper. The shape-controlling effects of the deposited copper atoms are finely balanced by tuning

the reduction rate of palladium ions via the addition of iodide anions to the growth solution. Previous work from our group showed that low micromolar concentrations of iodide ions facilitate palladium ion reduction during the synthesis of monometallic nanoparticles.[40] The deliberate incorporation of iodide in the current work similarly leads to an increased rate of palladium ion reduction, which in turn shifts the copper to palladium ratio of the particles at the key early stages of growth where shape is determined. Literature reports have shown that bimetallic palladium-copper particles tend to form alloyed tripod morphologies with higher copper content.[41, 42] In contrast, the cooperative effects of iodide and copper in this system direct particle formation to generate terraced bimetallic particles with a low copper content that suggests sub-monolayer copper coverage at the palladium surface. The absence of either copper or iodide results in low-index faceted morphologies or tripods, respectively. Together, these results represent a successful framework for enabling the use of copper underpotential deposition to control palladium nanoparticle shape.

Experimental

Chemicals

Hexadecyltrimethylammonium bromide (CTAB, BioXtra ≥ 99 %, lot no. SLBR1101V), L-ascorbic acid (ACS reagent, ≥ 99 %), sodium tetrachloropalladate (II) (Na_2PdCl_4, ≥ 99.99 % trace metal basis), and sodium borohydride ($NaBH_4$, granular, 99.99 %) were purchased from Sigma-Aldrich. Bis(p-sulfonatophenyl)phenylphosphine dihydrate dipotassium salt (BSPP, $C_6H_5P(C_6H_4SO_3K)_2 \cdot 2H_2O$, min. 97%) was purchased from STREM. Nitric acid concentrate (HNO_3, 100 mM), hydrochloric acid (HCl, TraceMetal™ Grade), nitric acid (HNO_3, TraceMetal™ Grade) and sodium iodide (NaI, Fisher Bioreagents, ≥ 99%) were purchased from Fisher Scientific. Copper (II) nitrate hydrate ($Cu(NO_3)_2 \cdot H_2O$, Puratronic 99.999% metal basis) was purchased from

Alfa Aesar. All chemicals were used without further purification and all solutions were prepared with deionized (DI) water (18.2 MΩ resistivity, Labconco Water Pro PS). Deactivated borosilicate glass wool (Restek, Cat. #20789) was purchased from Fisher Scientific and used without modification.

Synthesis of palladium seeds

In a typical synthesis, 0.250 mL of 10 mM Na_2PdCl_4 was added to 10.0 mL of 12.5 mM CTAB in a 20 mL scintillation vial with vigorous stirring, yielding a light brown solution. Upon thorough mixing, 0.600 mL of freshly prepared 10 mM $NaBH_4$ was rapidly injected, inducing an instantaneous darkening of the light brown solution. The seed solution was allowed to stir for an additional minute to ensure uniformity in the dispersion of the reducing agent. The stirring was then halted and the seed solution was allowed to sit for a period of two hours at room temperature.

Synthesis of terraced palladium-copper particles

After allowing the seed reaction to age, the resultant seed solution was then serially diluted by adding a 0.100 mL aliquot of the stock seed solution to 0.900 mL of 12.5 mM CTAB. From this solution, two subsequent ten-fold dilutions were made to obtain an aliquot of seeds that was 1,000x diluted relative to the original seed solution. This diluted seed solution was then set aside to be introduced to the growth solution in the final step. The growth solution was prepared by first adding 10.0 mL of 50 mM CTAB to a 20 mL scintillation vial and allowing the surfactant solution to equilibrate to 35 ^{o}C in a water bath. Following this equilibration, all other reactants were added to the 20 mL scintillation vial sequentially as follows with mixing after each addition: 0.500 mL of 10 mM Na_2PdCl_4, 0.020 mL of 10 mM $Cu(NO_3)_2$, 0.050 mL of 1 mM NaI. To generate particles with more defined terraces, 0.050 mL of 100 mM HNO_3 can also be added to the growth solution. To this growth solution, 0.100 mL of 100 mM ascorbic acid was then added and, finally, a 0.100

mL aliquot of the 1,000x diluted seed solution was injected to initiate particle growth, with initial color developing at approximately 45 minutes. The final color of the solution was grey with the particles settling at the bottom of the vial.

Materials characterization

Scanning electron microscopy (SEM) images were taken on a Hitachi SU-70 and a Hitachi SU-5000 field emission microscope. Scanning transmission electron microscopy (STEM) images and energy dispersive X-ray spectroscopy (STEM-EDS) maps were obtained using a FEI Tecnai Osiris 200kV TEM. A beryllium sample holder and gold TEM grids were used during collection of STEM-EDS maps to avoid interference from background copper signals. Samples for SEM and STEM-EDS imaging were prepared by centrifuging an aliquot of nanoparticles at 6,000 rpm for 4 minutes, removing the supernatant and then washing the particles with DI water. This washing process was repeated once more to remove excess surfactant. After the second wash the particles were resuspended in a small amount of water and then drop-cast onto a slice of silicon wafer (for SEM) or a gold TEM grid (for STEM-EDS).

Inductively coupled plasma mass spectrometry (ICP-MS) analysis was carried out using a Perkin Elmer ICP-MS Elan DRC-e. Separate but identical reaction solutions were used for each time point and were immediately quenched by injecting 0.100 mL of 55 mM BSPP followed by vigorous mixing to ensure uniform dispersion. A 1.0 mL aliquot was taken from each reaction vial and the samples were then centrifuged at 14,800 rpm for 10 minutes. The supernatant was removed with care to ensure the particles at the bottom of the tube were undisturbed. The particles were then washed with DI water and the previous procedure was repeated. After washing, the particles were resuspended in 1.0 mL of DI water which was then transferred to a 15 mL conical tube and digested with 2.0 mL of aqua regia (1:3 nitric acid to hydrochloric acid) made from concentrated

trace metal acids (Caution: strong acid). The particles were allowed to digest for several hours and were then carefully diluted to 10.0 mL with DI water.

X-ray photoelectron spectroscopy (XPS) spectra were collected using a monochromatic 1486.7 eV Al Kα X-ray source on a PHI VersaProbe II X-ray photoelectron spectrometer with 0.47 eV system resolution. Spectra were charge corrected to the C1s peak of adventitious carbon (284.8 eV). Samples were prepared on a slice of silicon wafer in a manner analogous to that used for SEM imaging, except that an entire 1 mL aliquot of particles was concentrated and drop-cast to generate a dense coverage of particles for XPS analysis.

Catalytic evaluation

Samples were prepared for catalytic evaluation by washing 80 mL of nanoparticle growth solution twice with water, centrifuging for 20 minutes at 7,830 rpm in 50 mL conical tubes each time. A concentrated solution of these nanoparticles was then mixed with a small piece of glass wool (~0.15 g). The nanoparticles were prepared for catalytic studies after six hours of growth, when particle formation was completed, to prevent galvanic exchange of surface copper. Catalysts were dried for at least four hours at 100 °C in an oven to remove water prior to catalytic testing. Dried catalysts were then placed into individual fritted quartz reactor tubes (0.4 inch internal diameter) and loaded into a flow reactor tube furnace. Reaction conditions for ethanol oxidation were 5% ethanol and 20% oxygen (O_2) with a total flow rate of 50 mL min^{-1} in helium (He) at 150 °C. Reaction products were monitored with an in-line gas chromatograph mass spectrometer (GC-MS, Agilent 7890B/5977A) and a thermal conductivity detector (TCD). Percent conversion and product selectivity were determined from the peak areas of species in the total ion chromatogram, with adjustment for MS ionization cross-sections.[43] ICP-MS of the catalysts post-reaction was used to determine catalyst mass for rate calculations.

Results and Discussion

Terraced palladium-copper nanoparticles were synthesized via a two-step seed-mediated method. Palladium seed particles were produced through the rapid reduction of sodium tetrachloropalladate (Na_2PdCl_4, 0.25 mL, 10 mM) in hexadecyltrimethylammonium bromide (CTAB, 10 mL, 50 mM) by injecting sodium borohydride (0.6 mL, 10 mM) with vigorous stirring and were subsequently aged for two hours at room temperature. A separate "growth solution" was prepared in the second step and consisted of Na_2PdCl_4 (0.5 mL, 10 mM), copper nitrate ($Cu(NO_3)_2$, 0.02 mL, 10 mM), sodium iodide (NaI, 0.05 mL, 1 mM), and ascorbic acid (0.1 mL, 100 mM) consecutively added to CTAB (10 mL, 50 mM) which had been preheated to 35 ^oC in a 20 mL scintillation vial. The mixture was swirled after each addition to ensure uniform mixing. Finally, particle growth was initiated through the injection of 0.1 mL of aged seed particles that had been serially diluted 1,000x in CTAB (12.5 mM) prior to injection. The growth solutions were allowed to react in a water bath at 35 ^oC and began to scatter light at approximately 45 minutes, causing the growth solution to appear grey-brown in color and indicating the onset of significant particle growth. The growth solutions were allowed to react overnight at 35 ^oC. Noticeable settling of particles to the bottom of the vials occurred over the course of the reaction indicating a final particle size greater than 50 nm. The final color of the reaction solution was predominantly grey. The prepared particles were characterized via scanning electron microscopy (SEM) to determine particle morphology and by inductively coupled plasma mass spectrometry (ICP-MS), X-ray photoelectron spectroscopy (XPS) and scanning transmission electron microscopy energy dispersive X-ray spectroscopy (STEM-EDS) to determine elemental composition.

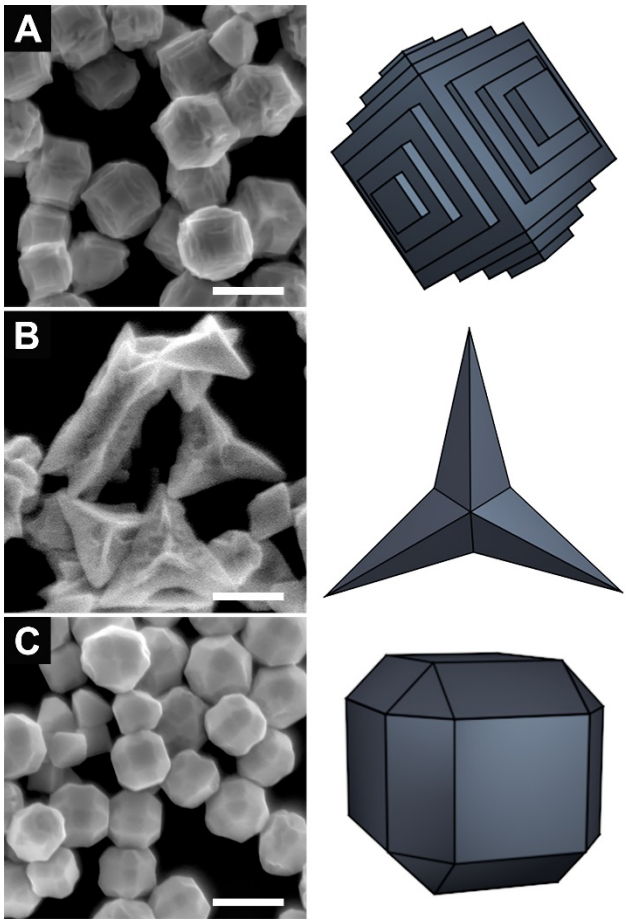

Fig. 1. Scanning electron microscopy (SEM) images and corresponding models representing (A) terraced cubes, (B) tripods, and (C) rounded cubes. The particles in (A) were synthesized with the addition of 0.05 mL of 100 mM nitric acid to improve definition of the surface features. Scale bars: 200 nm.

The resultant palladium-copper particles possess an underlying cubic structure with outward protrusions at each of the faces that form stepped terraces with a thickness on the order of a few nm (Fig. 1A, Fig. S1A-B and S2†). The emergence of these terraced surface features in the final particle morphology is critically dependent on the concentrations of both copper and iodide ions in the growth solution. The ideal concentrations of copper and iodide are 0.02 mM and 0.005 mM respectively. In the absence of iodide anions, the incorporation of copper leads to a mixture of multiply twinned particles including tripods, dendritic rods, and quasispherical particles with no distinct morphology (Fig. 1B, Fig. S1C†). Similarly, in the absence of copper, the incorporation

of iodide anions yields a cubic morphology with truncation at the edges and corners bound by a mixture of low-index facets (Fig. 1C, Fig. S1D†). Deliberate incorporation of iodide in this system drives the overall particle morphology towards a more prominent population of single crystalline low-index faceted structures rather than the polydisperse twinned dendritic structures that predominate when only copper is present to direct the shape. Overall, the incorporation of both copper and iodide in this growth system enables dual tuning of nanoparticle shape through both kinetic control, by using iodide to increase the rate of reduction of palladium ions, and selective surface passivation, in which edges and steps are stabilized through the underpotential deposition of copper. Together these two effects lead to the emergence of the terraced palladium-copper nanoparticles.

When the palladium ion reduction rates are probed via ICP-MS in the absence of copper, it becomes readily apparent that the rate of palladium ion reduction is drastically increased in the presence of iodide (Fig. 2A, Fig. S3†). One potential mechanism for this iodide-assisted reduction is an oxidation-reduction reaction between surface-bound iodide ions and palladium ions, in which iodide ions are oxidized to form triiodide and donate two electrons to reduce a palladium ion (Eq. 1).[40] Triiodide can then be reduced by ascorbic acid and re-adsorb to the palladium surface to

$$3I^- + Pd^{2+} \rightarrow I_3^- + Pd^0 \qquad \text{(Eq. 1)}$$

continue the cycle. Importantly, this rate increase leads to a distinct difference in the overall particle morphology. When iodide is omitted, the reaction yields multiply twinned structures that are bound by {100} facets, including right bipyramids and pentatwinned rods (Fig. 2B). In contrast, the incorporation of iodide directs growth toward largely single crystalline structures that have a rounded cubic morphology (Fig. 2C). The structures that result from these control experiments provide an understanding of a key aspect of the underlying shape evolution of the

more complex particles that form in the presence copper. The basic shape of the multiply twinned structures generated when only copper and palladium are present (i.e. in the absence of iodide) is analogous to that of the particles formed in the palladium-only control. Likewise, the ideal terraced structures that form when both copper and iodide are added can be related to the rounded cubic morphology from the palladium and iodide control. While the surface features of the copper-containing particles are different from the copper-free controls, this comparison of fundamental shape in the presence and absence of iodide indicates that the core morphology is dictated by the rate of palladium ion reduction.

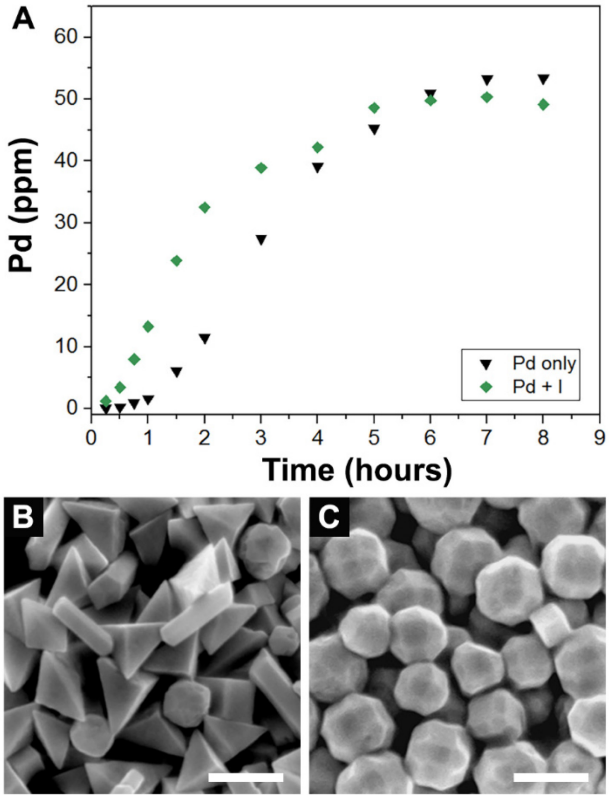

Fig. 2. (A) Graph of palladium incorporation during particle growth as determined by inductively coupled plasma mass spectrometry (ICP-MS) for palladium particles formed in the presence (green diamonds) and absence (black triangles) of iodide, (B) corresponding SEM image of palladium particles grown in the absence of iodide, and (C) corresponding SEM image of palladium particles grown in the presence of iodide. Scale bars: 200 nm.

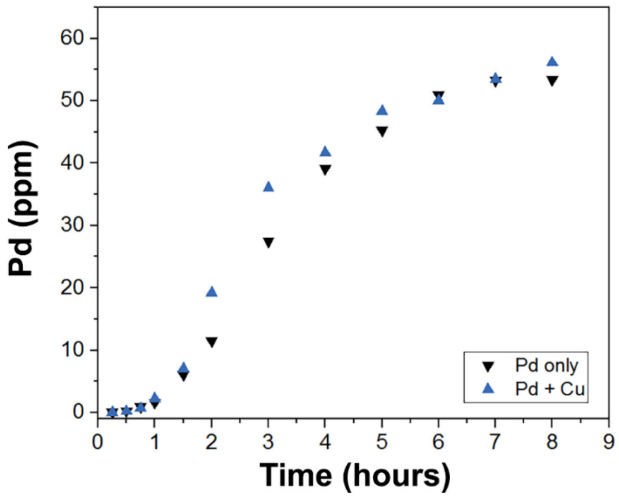

Fig. 3. Graph of palladium incorporation during particle growth as determined by ICP-MS for palladium particles formed in the presence (blue triangles) and absence (black triangles) of copper.

Investigation of the impact of copper on palladium ion reduction shows that the addition of copper alone does not affect the rate of reduction of palladium in this system, and suggests that copper has a surface passivating effect rather than a kinetic influence. Indeed, elemental analysis of the growth solution shows that the rates of reduction of palladium in the presence and absence of copper are almost identical (Fig. 3). Iodide, however, does slow the rate of copper ion reduction slightly, indicating that iodide has the ability to differentially control palladium and copper ion reduction. By comparing the rate of reduction of copper in the systems with and without iodide, it is readily apparent that the initial rate of copper ion reduction and therefore the initial incorporation of copper is greater in the system in which no iodide is present (Fig. 4A). Copper has a lower standard reduction potential than palladium: 0.60 V for $[PdCl_4]^{2-}$ compared to 0.34 V for Cu^{2+}, both vs. standard hydrogen electrode (SHE).[44] Therefore, since the standard potential for the reduction of triiodide to iodide is 0.536 eV vs. SHE,[44] iodide is not a strong enough reducing agent to reduce copper ions. The differential control of metal ion reduction rate provided by iodide anions enables an increase in palladium ion reduction rate while simultaneously slowing the rate of copper

ion reduction, which decreases the amount of copper in the terraced particles during the initial stages of growth. This is further evidence that the early formation of a larger palladium core is essential to the evolution of the terraced palladium-copper particles.

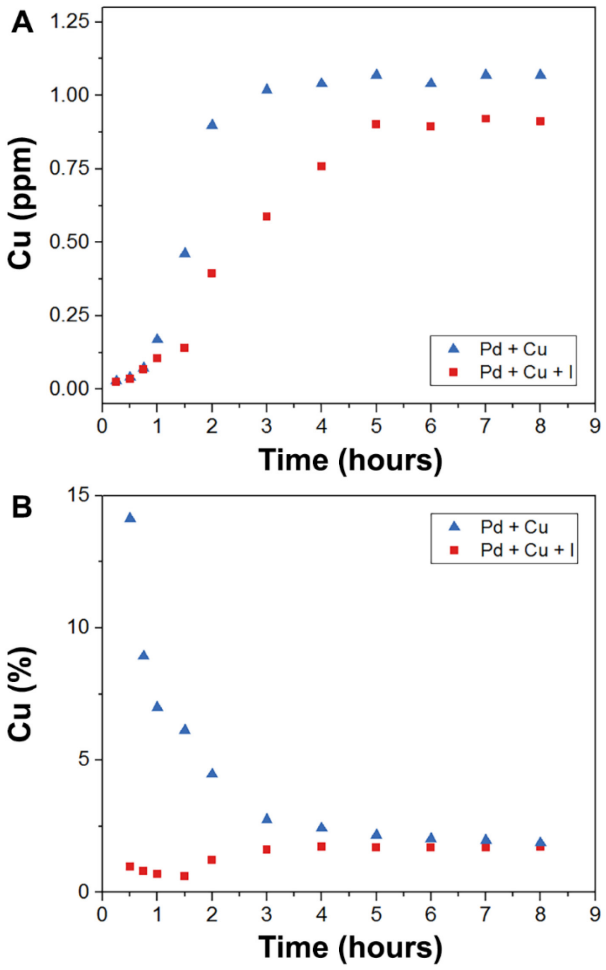

Fig. 4. Graphs of (A) copper incorporation and (B) composition during particle growth as determined by ICP-MS for palladium particles formed in the presence (red squares) and absence (blue triangles) of iodide.

Correlation of SEM images to the elemental analysis data at different time points confirms that the overall particle morphology with and without iodide is dictated by the relative rates of metal ion reduction early in the reaction (Fig. S4-S7†). In both cases, the final copper content of the palladium-copper particles is approximately 1-2%, but there is a noticeable difference in the copper content during the earlier time points (Fig. 4B). Indeed, the amount of copper that is

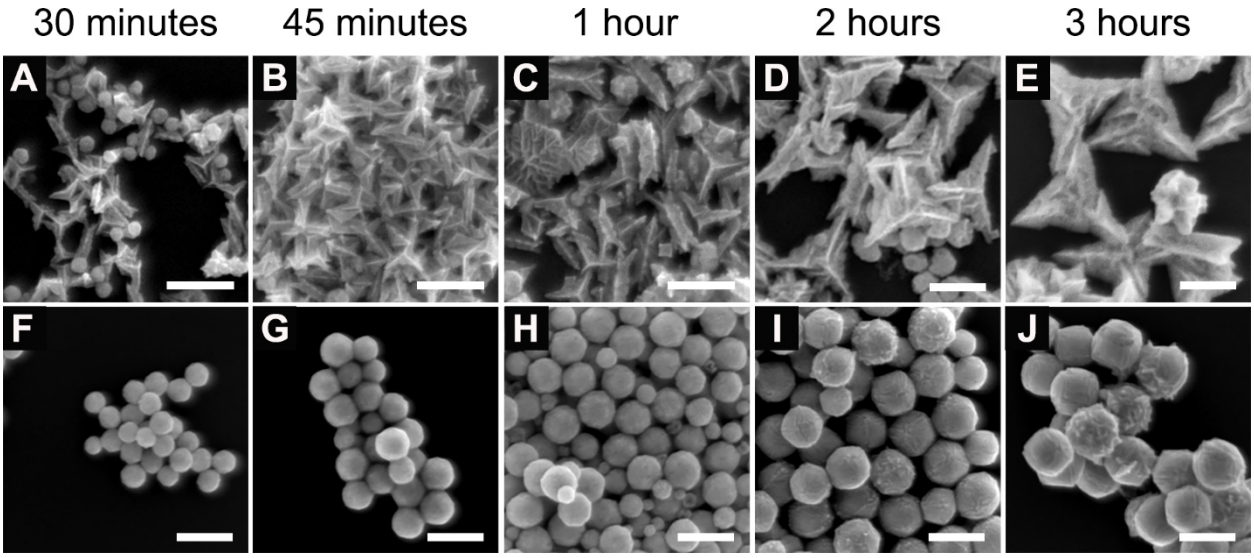

Fig. 5. SEM images of the formation of palladium-copper particles in the absence (A-E) and presence (F-J) of iodide at discrete time points (30 minutes, 45 minutes, 1 hour, 2 hours, and 3 hours.) Samples were obtained by quenching individual growth solutions with bis(p-sulfonatophenyl) phenylphosphine (BSPP). Scale bars: 200 nm.

incorporated in the absence of iodide during these early time points indicates a slightly faster initial deposition of copper that coincides with a significantly slower reduction of palladium and leads to an overall increased early copper content. When comparing the products of the palladium and copper growth solution at thirty minutes (Fig. 5A-E) to the growth solution containing iodide anions (Fig. 5F-J), the former yields multiply twinned particles with prominent growth at the edges and vertices which is evidence of likely copper deposition at these sites. Moreover, as the copper in these particles is galvanically replaced by palladium during the course of the reaction there is a distinct increase in definition at these sites as well as growth of ridges, resulting in the tripod and dendritic rod morphologies previously discussed. In contrast, increasing the rate of palladium ion reduction through the deliberate incorporation of low micromolar concentrations of iodide anions leads to an initial large core structure that appears to be single crystalline in nature. During later stages of particle growth, the copper is underpotentially deposited at the step edges of this structure, stabilizing edges and vertices. Copper is then galvanically replaced or otherwise

exchanged by its nobler palladium counterpart. Subsequent cycles of palladium deposition, underpotential deposition of copper, and exchange of copper with palladium persist through the rest of the growth period (Fig. 6). Importantly, the displacement of copper by palladium is slow relative to the direct deposition of palladium and the step sites are passivated relative to the terrace sites, thereby directing the formation of multilayered surface features.

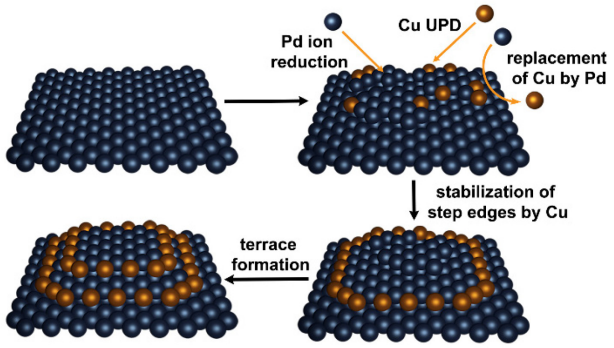

Fig. 6. Simplified schematic representation of the stabilization of palladium step sites by underpotentially deposited copper (Cu UPD), leading to the formation of terraces. The displacement of copper by palladium is slower than the direct reduction of palladium ions onto the particle surface, resulting in slowed growth outward from step sites. As a result, these copper-passivated steps are maintained in the final particle morphology.

This mechanistic description of particle growth is supported by XPS analysis of the surfaces of the nanoparticles formed under each of the different growth conditions (Fig. 7, Fig. S8†). High-resolution spectra of the copper 2p region for the palladium-copper particles formed in the absence of iodide indicates that no copper is present at the surface of the particles (Fig. 7A). This is likely a consequence of the rapid reduction of copper early in particle growth followed by subsequent galvanic exchange of copper by palladium. This lack of copper at the particle surface is also supported by elemental mapping of the particles via EDS (Fig. S9†), which suggests that the copper in these particles is more localized in the core as a copper-palladium alloy surrounded by a palladium shell. However, it is important to note that the bulk copper content for these particles approaches the limit of detection for EDS (approximately 1%) and submonolayer coverages of

copper are not mappable using this approach. Therefore, the XPS results are more conclusive in determining surface composition. In contrast, for the terraced particles, in which the onset of copper deposition is delayed, copper is still present at the particle surface at the conclusion of particle growth (Fig. 7A). The surface coverage of copper in these particles is low, which is expected for submonolayer formation through underpotential deposition. EDS mapping shows copper extending to the surface of the particles (Fig. S10-S11†), though, as before, the submonolayer coverage is too dilute to map conclusively using this technique. Interestingly, according to XPS characterization, the coverage of iodide at the surface of the terraced particles is low in comparison to the monometallic palladium particles formed in the presence of iodide (Fig. 7B). This suggests that the coverage of iodide at the particle surface is high at early stages of growth, thereby contributing to enhanced palladium ion reduction and the formation of a single crystalline core, and that it is largely displaced by copper at later stages of growth.

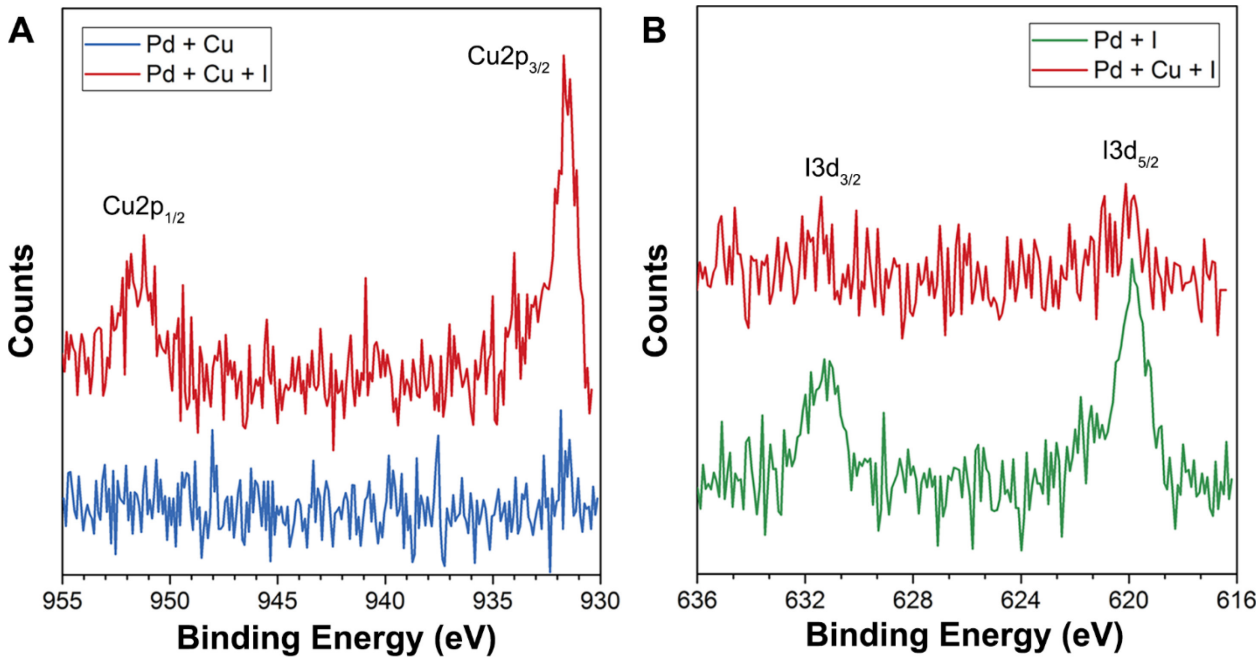

Fig. 7. High-resolution XPS spectra of (A) the copper 2p region for palladium-copper particles formed in the absence and presence of iodide and (B) the iodide 3d region for palladium and palladium-copper particles formed in the presence of iodide. Particles were prepared for analysis after 6 hours of reaction, when particle growth is complete.

The terraced particles can be tuned to have sharper edges and vertices through the addition of nitric acid to the growth solution to slow the reduction of both metal ions by decreasing the reducing power of ascorbic acid. Further decreasing the pH through the incorporation of additional nitric acid has a drastic impact on overall particle morphology even though all other conditions are held constant. In the absence of nitric acid, the ideal copper and iodide concentrations yield a large proportion of the terraced palladium and copper nanoparticles that are approximately 175 nm in size (Fig. 8A). The addition of 25 or 50 μL of 100 mM nitric acid under otherwise identical conditions—Figs. 8B and 8C, respectively—gives rise to enhanced definition of the terraces. The emergence of sharper features is not unexpected, as the onset of copper underpotential deposition is shifted to later time points, leading to a larger overall particle size which stabilizes sharp features at the particles' surface by increasing the radius of curvature of the terrace edges (Fig. S12†).

Further increasing the volume of acid added to 75 µL results in particles that are considerably more rounded and exhibit greater proportions of {111} surface features, which suggests a change in the mechanism of growth (Fig. 8D). Indeed, the addition of 100 – 175 µL of nitric acid (Fig. 8E-H) leads to a complete shift toward the evolution of concave octahedra rather than terraced cubes. These concave octahedral particles resemble monometallic palladium particles reported in the presence of iodide,[45] suggesting that ascorbic acid is no longer strong enough to reduce copper via underpotential deposition.

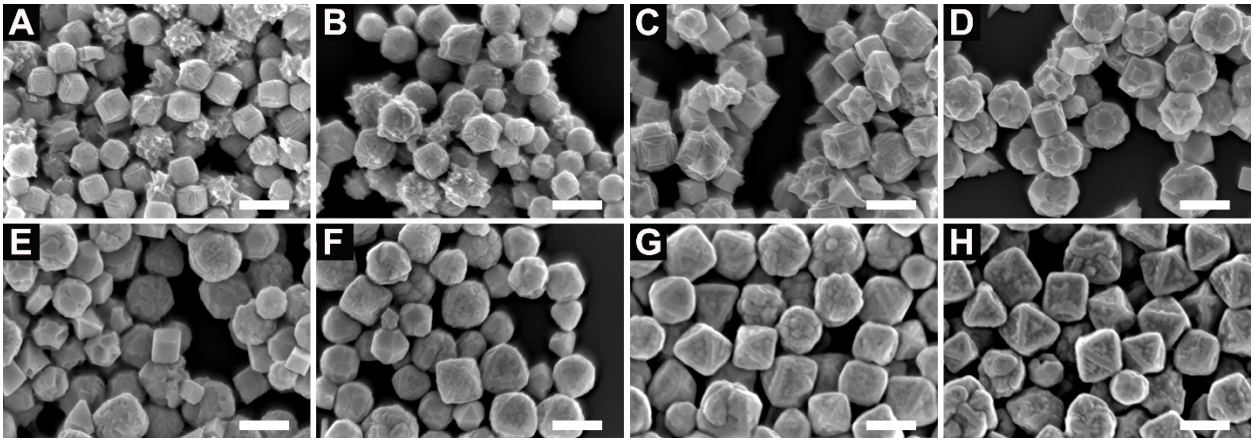

Fig. 8. SEM images illustrating a distinct change in particle morphology from terraced palladium-copper particles to concave octahedra with increasing amounts of 100 mM nitric acid in the growth solution: (A) no acid; (B) 25 µL of HNO_3; (C) 50 µL of HNO_3; (D) 75 µL of HNO_3; (E) 100 µL of HNO_3; (F) 125 µL of HNO_3; (G) 150 µL of HNO_3; and (H) 175 µL of HNO_3. Scale bars: 200 nm.

To probe this trend more thoroughly, the elemental composition of these bimetallic structures at different growth stages was analyzed in the presence of 0, 50, and 175 µL of 100 mM nitric acid to determine the underlying cause of the shape change (Fig. 9). As hypothesized, the resultant concave octahedral shaped particles that form in the presence of 175 µL of nitric acid have no copper content throughout the entire reaction (Fig. 9B). The incorporation of nitric acid weakens the reducing power of ascorbic acid, preventing the reduction of copper completely, and results in

particles that possess a concave octahedral morphology that forms when copper is omitted from the growth solution under analogous conditions (Fig. S13†). Similarly, when 50 µL of acid is present in the growth solution there is a slight decrease in the rate of copper reduction (Fig. 9B), however, the observed reduction of palladium occurs at close to the same rate as the experiments where no acid is present (Fig. 9A). This slight slowing in the rate of copper ion reduction leads to faster core growth yielding a larger overall particle morphology that is better able to stabilize sharper edge features.

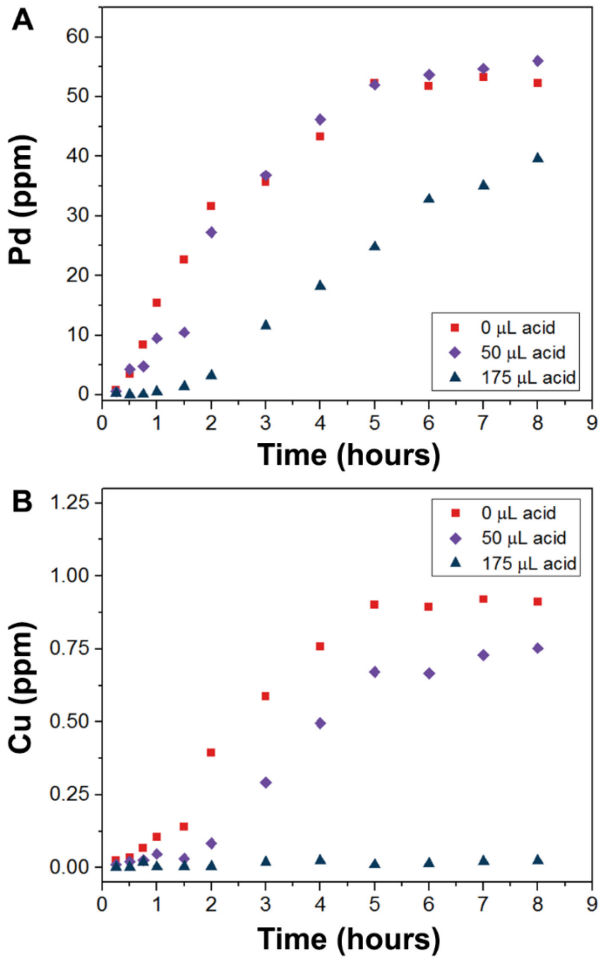

Fig. 9. Graphs of (A) palladium and (B) copper incorporation during particle growth as determined by ICP-MS for particles formed with increasing volumes of added 100 mM nitric acid.

The catalytic performance of these terraced copper-palladium nanoparticles for the gas phase oxidation of ethanol was evaluated and compared to the monometallic palladium nanoparticles synthesized in the presence and absence of iodide to probe the effects of changes in surface structure and composition on the catalytic behavior of these materials. Each of the nanoparticle materials was dispersed and dried on deactivated glass wool as an inert support, and catalytic experiments were carried out under flowing, ambient pressure conditions. Three oxidation products were observed: acetaldehyde, ethyl acetate, and acetic acid (Fig. S14-15†). While the {100}-faceted palladium nanoparticles synthesized in the absence of iodide exhibited the highest overall activity (0.33 mmol s^{-1} g^{-1} relative to 0.20 mmol s^{-1} g^{-1} for the palladium nanoparticles synthesized with iodide and 0.21 mmol s^{-1} g^{-1} for the terraced palladium-copper nanoparticles), the palladium-copper nanoparticles were the most selective to a single product. At comparable conversions of close to 16% (15.6-16.2%), the terraced palladium-copper particles were 93.4% selective to acetaldehyde, with the remaining product being the oxidative coupling product, ethyl acetate (Fig. 10A). In contrast, the oxidation of ethanol over palladium nanoparticles with and without iodide at the surface yielded acetic acid in addition to acetaldehyde and ethyl acetate. The monometallic palladium particles with no iodide showed 76.8% selectivity to acetaldehyde production, with 18.5% selectivity to ethyl acetate and a small amount of acetic acid formation (4.7% selectivity). Interestingly, when compared to the palladium nanoparticles without iodide, the palladium nanoparticles with surface iodide had a greater selectivity to acetic acid (8.2%), along with a higher selectivity to acetaldehyde (81.4%) and a lower selectivity to ethyl acetate (10.4%). At the maximum observed conversions, the selectivity to acetaldehyde for the terraced copper-palladium particles decreased slightly, to 86.9% (Fig. 10B). The selectivity to acetaldehyde for the palladium particles with iodide decreased more significantly, to 71.7%, while that of the

palladium particles with no iodide decreased dramatically, to 53.5%, coupled with a significant increase in ethyl acetate and acetic acid production.

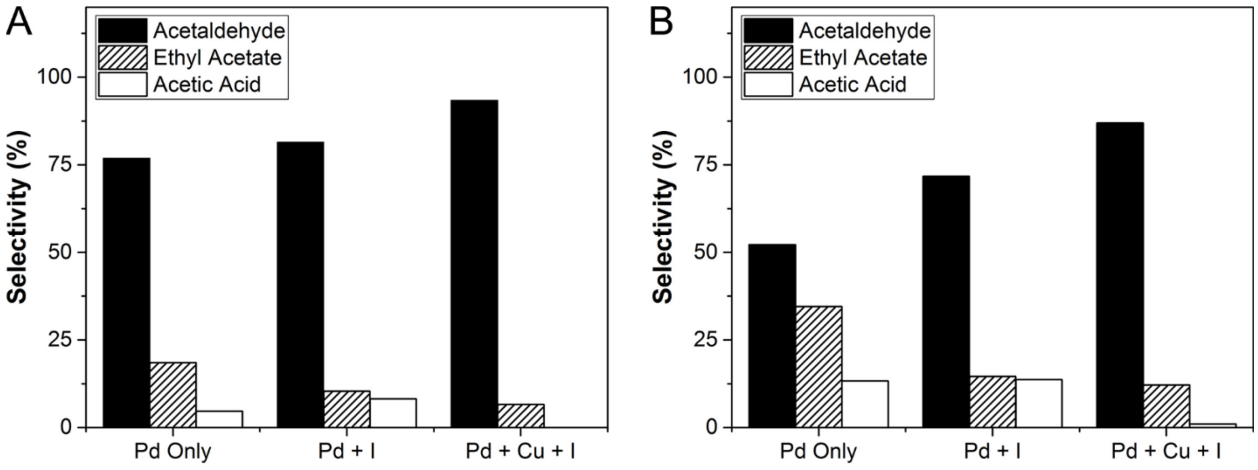

Fig. 10. Graphs of product selectivity at (A) approximately 16% conversion and (B) maximum conversion in the catalytic oxidation of ethanol by palladium nanoparticles synthesized with and without iodide as well as palladium-copper terraced particles synthesized with the addition of 50 μL of 100 mM nitric acid. Reaction conditions: 5% ethanol and 20% O_2 in He (50 mL min^{-1}), 150 °C, 1.9-2.5 mg of catalyst.

Together, these results suggest that copper at the surface of the terraced palladium-copper nanoparticles is passivating a portion of the active surface sites and modifying the activity of palladium to decrease the production of ethyl acetate and acetic acid. While the presence of iodide at the palladium surface does decrease formation of ethyl acetate to some extent, it does not prevent acetic acid formation. Thus, the addition of iodide alone is not sufficient to account for the increased selectivity of the terraced particles toward acetaldehyde. This indicates that surface copper is necessary to inhibit acetic acid formation. Similar suppression of acetic acid formation by copper has also been observed for small, spherical palladium-copper alloys.[46] The ability of the terraced palladium-copper nanoparticles to maintain a significant conversion rate while also exhibiting enhanced selectivity points to the broader potential opportunities for dilute bimetallic nanoparticles with high-energy surfaces in tailoring catalyst performance.

Conclusion

Overall, this work highlights the utility of iodide ions as a tool for differentially tuning the reduction rates of two dissimilar metal ion precursors, here palladium and copper. This is a degree of control that is not achievable with most standard methods of modifying metal ion reduction rates, such as adjusting the solution pH, raising or lowering the reaction temperature, or changing the surfactant counterion. In the current system, by adding a low micromolar concentration of iodide ions to the nanoparticle growth solution, it is possible to increase the rate of palladium ion reduction while simultaneously decreasing the rate of copper ion reduction, thereby reaching the optimum relative reduction rates for enabling the copper underpotential deposition driven formation of terraced palladium-copper nanostructures. The resulting submonolayer coverage of copper at the surface of these terraced nanoparticles enhances their selectivity in the catalytic gas phase oxidation of ethanol by blocking pathways to acetic acid production. This approach also has the potential to be more broadly applicable to the synthesis of other dilute bimetallic nanomaterials involving a more easily reduced noble metal and a more catalytically active but less easily reduced non-noble transition metal. Work to expand the scope of this iodide-assisted method is ongoing in our research group. Nanostructures that are bound by well-defined surface facets and have mixed noble metal/non-noble metal compositions are of significant interest in fundamental research focused on enhancing selectivity and sustainability in catalytic transformations. This work provides a promising new avenue for addressing the significant synthetic challenges inherent in generating such complex functional materials.

Conflicts of interest

There are no conflicts of interest to declare.

Acknowledgements

Acknowledgement is made to the donors of The American Chemical Society Petroleum Research Fund for partial support of this research. This work was also supported by start-up funding from Wesleyan University. SEM imaging at Wesleyan University was supported by the National Science Foundation Major Research Instrumentation program under Grant No. 1725491. STEM-EDS and additional SEM characterization carried out at Yale University were supported by YINQE and NSF MRSEC DMR 1119826. ICP-MS measurements were performed at the Yale Analytical and Stable Isotope Center (YASIC), a Yale Institute for Biospheric Studies (YIBS) research center. XPS analysis was conducted at the Yale University West Campus Materials Characterization Core and the authors thank Dr. Min Li for assistance in acquiring the XPS spectra.

† Electronic supplementary information (ESI) available.

Notes and references

1. N. Zhou, V. Lopez-Puente, Q. Wang, L. Polavarapu, I. Pastoriza-Santos and Q.-H. Xu, *RSC Adv.*, 2015, **5**, 29076-29097.
2. M. A. Boles, M. Engel and D. V. Talapin, *Chem. Rev.*, 2016, **116**, 11220-11289.
3. S. Chavez, U. Aslam and S. Linic, *ACS Energy Lett.*, 2018, **3**, 1590-1596.
4. S. Linic, P. Christopher and D. B. Ingram, *Nat. Mater.*, 2011, **10**, 911-921.
5. D. Schaadt, B. Feng and E. Yu, *Appl. Phys. Lett.*, 2005, **86**, 063106.
6. H. Zhang and A. O. Govorov, *J. Phys. Chem. C*, 2014, **118**, 7606-7614.
7. K. An and G. A. Somorjai, *ChemCatChem*, 2012, **4**, 1512-1524.
8. S. Linic, P. Christopher, H. Xin and A. Marimuthu, *Acc. Chem. Res.*, 2013, **46**, 1890-1899.
9. L. Liu and A. Corma, *Chem. Rev.*, 2018, **118**, 4981-5079.
10. B. Roldan Cuenya and F. Behafarid, *Surf. Sci. Rep.*, 2015, **70**, 135-187.
11. Z. Wang, H. Wang, Z. Zhang, G. Yang, T. He, Y. Yin and M. Jin, *ACS Nano*, 2017, **11**, 163-170.
12. J. Zhang, Q. Kuang, Y. Jiang and Z. Xie, *Nano Today*, 2016, **11**, 661-677.
13. D. Kim, C. Xie, N. Becknell, Y. Yu, M. Karamad, K. Chan, E. J. Crumlin, J. K. Nørskov and P. Yang, *J. Am. Chem. Soc.*, 2017, **139**, 8329-8336.
14. L. Zhang, Z. Xie and J. Gong, *Chem. Soc. Rev.*, 2016, **45**, 3916-3934.
15. L. Zhang, Q. Chen, X. Wang and Z. Jiang, *Nanoscale*, 2016, **8**, 2819-2825.
16. S. Rej, C.-F. Hsia, T.-Y. Chen, F.-C. Lin, J.-S. Huang and M. H. Huang, *Angew. Chem. Int. Ed.*, 2016, **55**, 7222-7226.
17. X. Li, X. Wang, M. Liu, H. Liu, Q. Chen, Y. Yin and M. Jin, *Nano Res.*, 2018, **11**, 780-790.

18. A. Zaleska-Medynska, M. Marchelek, M. Diak and E. Grabowska, *Adv. Colloid Interface Sci.*, 2016, **229**, 80-107.
19. W. Yu, M. D. Porosoff and J. G. Chen, *Chem. Rev.*, 2012, **112**, 5780-5817.
20. M. Morad, E. Nowicka, M. Douthwaite, S. Iqbal, P. Miedziak, J. K. Edwards, G. L. Brett, Q. He, D. Morgan, H. Alshammari, D. Bethell, D. W. Knight, M. Sankar and G. J. Hutchings, *Catal. Sci. Technol.*, 2017, **7**, 1928-1936.
21. M. Laskar and S. E. Skrabalak, *J. Mater. Chem. A*, 2016, **4**, 6911-6918.
22. C. Roychowdhury, F. Matsumoto, V. B. Zeldovich, S. C. Warren, P. F. Mutolo, M. Ballesteros, U. Wiesner, H. D. Abruña and F. J. DiSalvo, *Chem. Mater.*, 2006, **18**, 3365-3372.
23. D. D. Robertson, M. E. King and M. L. Personick, *Top. Catal.*, 2018, **61**, 348-356.
24. J. Gu, Y.-W. Zhang and F. Tao, *Chem. Soc. Rev.*, 2012, **41**, 8050-8065.
25. Q. Chen, Y. Jia, S. Xie and Z. Xie, *Chem. Soc. Rev.*, 2016, **45**, 3207-3220.
26. K. D. Gilroy, A. Ruditskiy, H.-C. Peng, D. Qin and Y. Xia, *Chem. Rev.*, 2016, **116**, 10414-10472.
27. R. G. Weiner, M. R. Kunz and S. E. Skrabalak, *Acc. Chem. Res.*, 2015, **48**, 2688-2695.
28. L. Han, P. Cui, H. He, H. Liu, Z. Peng and J. Yang, *J. Power Sources*, 2015, **286**, 488-494.
29. M. Gong, G. Fu, Y. Chen, Y. Tang and T. Lu, *ACS Appl. Mater. Interfaces*, 2014, **6**, 7301-7308.
30. J. Chen, B. Wiley, J. McLellan, Y. Xiong, Z.-Y. Li and Y. Xia, *Nano. Lett.*, 2005, **5**, 2058-2062.
31. H. Jing and H. Wang, *Chem. Mater.*, 2015, **27**, 2172-2180.
32. K. D. Gilroy, P. Farzinpour, A. Sundar, R. A. Hughes and S. Neretina, *Chem. Mater.*, 2014, **26**, 3340-3347.
33. L. Zhang, J. Zhang, Q. Kuang, S. Xie, Z. Jiang, Z. Xie and L. Zheng, *J. Am. Chem. Soc.*, 2011, **133**, 17114-17117.
34. O. A. Oviedo, P. Vélez, V. A. Macagno and E. P. M. Leiva, *Surf. Sci.*, 2015, **631**, 23-34.
35. J. Zhang, M. R. Langille, M. L. Personick, K. Zhang, S. Li and C. A. Mirkin, *J. Am. Chem. Soc.*, 2010, **132**, 14012-14014.
36. L. Zhang, Q. Chen, Z. Jiang, Z. Xie and L. Zheng, *CrystEngComm*, 2015, **17**, 5556-5561.
37. M. R. Langille, M. L. Personick, J. Zhang and C. A. Mirkin, *J. Am. Chem. Soc.*, 2012, **134**, 14542-14554.
38. M. Liu and P. Guyot-Sionnest, *J. Phys. Chem. B*, 2005, **109**, 22192-22200.
39. T. Ming, W. Feng, Q. Tang, F. Wang, L. Sun, J. Wang and C. Yan, *J. Am. Chem. Soc.*, 2009, **131**, 16350-16351.
40. M. E. King and M. L. Personick, *Part. Part. Syst. Char.*, 2017, **34**, 1600422.
41. L. Zhang, S.-I. Choi, J. Tao, H.-C. Peng, S. Xie, Y. Zhu, Z. Xie and Y. Xia, *Adv. Funct. Mater.*, 2014, **24**, 7520-7529.
42. Y.-T. Chu, K. Chanda, P.-H. Lin and M. H. Huang, *Langmuir*, 2012, **28**, 11258-11264.
43. B. Xu, R. J. Madix and C. M. Friend, *J. Am. Chem. Soc.*, 2010, **132**, 16571-16580.
44. A. J. Bard, R. Parsons and J. Jordan, *Standard Potentials in Aqueous Solution*, Marcel Dekker, New York, 1985.
45. W. Niu, L. Zhang and G. Xu, *ACS Nano*, 2010, **4**, 1987-1996.
46. J. Yin, S. Shan, M. S. Ng, L. Yang, D. Mott, W. Fang, N. Kang, J. Luo and C.-J. Zhong, *Langmuir*, 2013, **29**, 9249-9258.

Table of Contents

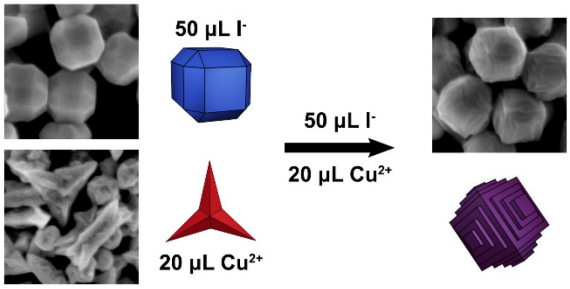

Iodide-induced kinetic control enables selective surface passivation of palladium through underpotential deposition of copper to generate terraced palladium-copper particles.